RSC Advances

ROYAL SOCIETY OF CHEMISTRY

www.rsc.org/advances

Novel TiO_2 /Graphene Oxide Functionalized with Cobalt Complex for Significant Degradation of NO_x and CO

N. Seifvand[a], E. Kowsari [a*]

[a] Department of Chemistry, Amirkabir University of Technology, Hafez Avenue, No. 424, Tehran, Iran, Fax: +98(21)64543296, Tel.: +98(21)64543295, E-mail: kowsarie@aut.ac.ir

Abstract

We are releasing a well-designed nanostructured composite, consisting of titanium dioxide (TiO_2) and cobalt (Co) imidazole (Im) complex functionalized graphene oxide (FGO). Co-Im complex was attached on the GO by covalence bonding of Im with graphene functional groups. Films were characterized by XRD, XPS, TEM, UV-Vis, FTIR and Raman spectroscopy in order to subsequently prove the evidence of hybridization GO with Co-Im complex. Band gap calculated for the TiO_2 thin film was 3.10 eV, 2.96 for TiO_2/GO and 2.776 for TiO_2/FGO. Experimental results confirmed high-percentage deterioration of NO_x (51%) and CO (46%). The photodegradation experiments revealed significant photocatalytic character of TiO_2, physical adsorption of GO, and the affinity of cobalt to complex formation with pollutant gases. The TiO_2/FGO composite modifies air-pollutant degradation by nearly three times more than the bare TiO_2 thin film.

1. Introduction

Currently, human beings have a severe problem called air pollution, particularly contributing to asthmatic diseases, children and old people who live in populated cities. Gases such as NO_x (NO, NO_2) and CO are toxic and have many dreadful impacts on public health such as cancers.[1–5]

National Ambient Air Quality Standards (NAAQS) have limited maximum indoor level of carbon monoxide 35 ppm and for Nitrogen dioxide 100 ppb (in 1-hour).[6,7] Scientists offered and used different techniques for the removal of NO_x and CO. Selective catalytic reduction

(SCR) has been proposed with high amount of NO elimination; however, the procedure is cost-effective and requires elevated temperatures.[8–10]

NO_x and CO are difficult to oxidize and remove; consequently, it is essential to implement new and economical methods for their destruction. Photocatalysis could be one alternative, because they have low price and efficiency, the energy source (both solar and artificial) is light, catalysts are not toxic (semiconductors such as TiO_2), and the decomposition products are harmless (CO_2 and H_2O).[11] Fujishima and Honda explored the photocatalytic nature of TiO_2,[12] which is preferable to other semiconductor oxides because of its chemical stability, low cost and lack of toxicity.[13,14] Detailed mechanisms of TiO_2 photochemical reactions are well documented.[15–17]

Successful synthesis of TiO_2 photocatalyst is essential for achieving the best photocatalytic activity. We have selected film instead of powder form, because of its superior properties like optical transparency, further mechanical stability; durability and adhesion on the surface. Additionally, thin film can be easily separated and assembled for regeneration or replacement purposes.[18-23]

TiO_2 thin films could be arranged by numerous methods, such as sol-gel,[24,25] hydrothermal,[26] anodizing Ti foil,[27] chemical vapor deposition,[28] metal–organic chemical vapor deposition,[29] pulsed laser deposition[30] and RF magnetron sputtering,[31] with diverse crystalline structure that greatly relies on the preparation method. Among them, RF magnetron sputtering is one of the easiest to industrialize.[32] This technique is suitable for optical coatings, owing to its high density, high adhesion, hardness and uniformity.[33]

TiO_2 in anatase form demonstrates photocatalytic activity only after UV light irradiation (λ<384 nm).[34,35] Practical composites may be created to overcome large band gap of TiO_2 (3.2 eV). Li et al. proved that combining carbon nanotubes (CNTs) with TiO_2 could assist in the separation of electron–hole charges.[36] Choy et al. reported TiO_2/clay composite with excellent photocatalytic activity.[37] TiO_2 composited with zeolite templated carbon (TiO_2–ZTC) successfully adsorbed organic molecules according to its high surface area.[38] TiO_2 composited with mesoporous silicate MCM-41 exhibited good photocatalytic activity for oxidizing phenol.[39] Hybrid SiO_2-TiO_2 material has been synthesized and characterized as a composite with tunable surface area (500–1170 $m^2\ g^{-1}$); [40] however, in our case, we needed a composite with the ability of surface functionalization to handle both photocatalytic activity and complex formation with pollutants. Graphene oxide (GO) is our choice to make composite due to its high surface area, non-toxicity and functionability. GO is analogue to benzene and polycyclic aromatic hydrocarbons, consisting of sp^2 and sp^3 carbon atoms.[41-43]

GO as an absorbent, owing to its large theoretical surface area (2630 m^2g^{-1}), is very fascinating. As a result, GO is potentially applicable in the environmental remediation as an effective sorbent for pollutants. Recently, GO has been used to remove MB,[44] fluoride,[45,46] aromatics,[47-49] dyes,[50,51] arsenic[52] and other heavy metals from aqueous solutions, with high adsorption amounts and fast adsorption rates.[53,54]

GO is capable for functionalization through its alcohol, epoxide, carboxyl and ketone groups, properly.[55–57] Chemically modified graphenes (CMGs) have been achieved by adding functional groups to GO.[58-63] Prior to our research, only a few cases of research employing semimetals or metals were released on CMGs.[64,65] Functionalization of GO with cobalt has been used for various applications like unusual catalytic effect,[66] enhanced photocatalytic H_2 production[67] and ameliorated electrochemical performances.[68] Furthermore, in particular, cobalt has attracted extensive attention because of its outstanding properties like being earth-abundant metal,[69] interfacial hole transfer promotion, and consequently band gap reduction,[70,71] and above all, Co(II) ions being excellent metal centers in complex formation with NO_x and CO.[72] Interactions between cobalt and gases such as CO and NO lead to complex formation, and thereby gaseous pollutants are eliminated.[73-75]An effective approach is to fabricate transition metal compounds for complex formation with NO and CO ligands on the GO surface.

As a matter of fact, this paper deals with the synthesis of a composite photocatalyst in the form of a thin film, consisting of TiO_2 synthesized by RF magnetron sputtering on a quartz surface with uniform thickness; subsequently, functionalized GO with cobalt imidazole complex is deposited on the TiO_2 surface with the purpose of air purification.

2. Experimental

2.1. Synthesis

2.1.1. Preparation of the TiO_2 Thin Film

The TiO_2 thin film was prepared using the RF magnetron sputtering method with a Ti target (Grade: 99.99%, diameter: 100 mm, thickness: 5 mm) as the source material, Ar (99.995%) was the sputtering gas and O_2 (99.995%) was the reactive gas. Unheated substrates were performed for deposition. RF generator operated at the frequency of 13.56 MHz and 200 W. Turbo pump was utilized for vacuuming stainless-steel chamber with the pressure less than 2.7×10^{-3} Pa. Mixed gases of Ar and O_2 purged to the vacuum chamber with the pressure

ratio of 9:1 while the total pressure was 1.1 Pa. Before the deposition, the chamber was kept in the pre-sputtering period for 20 min for the purpose of removing contaminants and stabilizing the deposition parameters.

Quartz substrates were ultrasonically washed with acetone, ethanol and deionized water, each for 15 min. After the substrates were cleaned, they were placed on a sample holder facing the target at a fixed distance of 50 mm in a vacuum chamber. TiO_2 film with a thickness of 900 nm was deposited onto each quartz substrate. In our experiment, the deposition rate was 2.5–5.8 nm/min and the deposition time was approximately 160 min. The deposited films were annealed at 550°C for 1 h in air.

2.1.2. Preparation of GO

The adjusted Hummers method was employed to oxidize graphite.[76] H_2SO_4 (50 mL) was added into a 500 mL flask containing graphite (2 g) and $NaNO_3$ (1 g) at 0°C in an ice bath. $KMnO_4$ (6 g) was added to the above mixture, slowly (over 1 h) to prevent the temperature increasing. The suspension was stirred continuously for 2 h, diluted with 350 mL of deionized water, and left for 2 days before H_2O_2 (30%) was added in order to reduce any residual manganese dioxide and permanganate and to soluble manganese sulfate. This mixture was filtered with a glass filter, followed by washing with dilute HCl (10% vol). GO was dried under vacuum at ambient temperature.

2.1.3. Acylation of GO

GO was acylated with thionyl chloride ($SOCl_2$) to introduce acyl chloride groups on the surface. Acyl-chloride-modified GO was prepared by reacting GO (0.2 g) with $SOCl_2$ (85 mL) and dimethylformamide (DMF; 4 mL) at 70°C for 24 h inside a dry Ar glove box to activate the carboxylic units by forming the corresponding acyl chlorides. The reaction took place between the C=O in carboxyl and chloride ions (Eq. 1). Anhydrous tetrahydrofuran (THF) was used to remove excess oxalyl chloride from the remaining acyl-chloride-functionalized GO (GO–COCl), and then the product was washed with anhydrous toluene for three times. The resulting solid material was centrifuged and dried at room temperature under vacuum.

$$SOCl_2 + RCO_2H \rightarrow RC(O)Cl + SO_2 + HCl \quad (1)$$

2.1.4. Modification of GO with Imidazole

Acyl-chloride-functionalized GO (0.2 g) was re-dispersed in DMF (40 mL) in dry Ar-filled glove box and dry conditions with excess imidazole (1 g) and refluxed at 70°C for 72 h. Imidazole ($C_3H_4N_2$) is a weak base with two N atoms, which was chemically deposited onto the resulting acylated GO through an acid–base reaction. The resulting brown–gray solid was separated by filtration. The product was washed with methylene chloride (4 × 20 mL) and dried under vacuum (See Supplementary Information Figure S1).

2.1.5. Functionalized GO with Cobalt Complex

GO functionalized with cobalt was obtained from the reaction of imidazole-functionalized GO with $CoCl_26H_2O$ (0.1 mmol, 2.379 g) in methanol (50 mL). The mixture was refluxed for 1 h and then reserved for a few days at atmospheric temperature; pink cobalt-complex crystals emerged. A cobalt tetrakis imidazole chloride complex $[Co(Im)_4]Cl_2$ was obtained (See Supplementary Information Figure S2).

2.1.6. Deposition of Functionalized GO on TiO_2

Functionalized GO (FGO) was suspended in ethylene glycol (1mg/mL). Then, the solution was subjected to ultrasonication with a probe-type sonicator for 2 h in order to obtain a uniform aqueous solution. The FGO suspension was spin-coated at 2000 rpm for 30 s with a HOLMARC Spin coater-model: HO-TH-05 on TiO_2-sputtered quartz to achieve a 30±2 nm FGO film thickness.[77] (See Supplementary Information Figure S3).

2.2. Reagents

Graphite (powder, <45 μm, ≥99.99%, Sigma-Aldrich), potassium permanganate ($KMnO_4$, 158.03 g/mol, extra pure; Merck), sulfuric acid (H_2SO_4 95%, extra pure, Merck), hydrogen peroxide (H_2O_2 30%, Merck), sodium nitrate ($NaNO_3$, 84.99 g/mol, ≥99.0%, Merck) imidazole ($C_3H_4N_2$, 68.08 g/mol ≥99%, Sigma-Aldrich) cobalt chloride ($CoCl_26H_2O$, 237.90 g/mol ≥98%), methanol (CH_4O 32.04 g/mol, Merck) THF (C_4H_8O 72.11 g/mol, Merck), thionyl chloride ($SOCl_2$, 99.5% , 118.97 g/mol, Sigma-Aldrich), and dilute hydrochloric acid (HCl 37% Merck diluted in H_2O) were used in this work.

2.3. Instrumentation

Crystal structure of TiO_2 thin film was characterized by X-ray diffraction with Cu radiation (X'Pert Pro MPD, PANalytical). Accelerating voltage and applied current were 40 kV and 40 mA, respectively and an incident angle of 1°C was used in the region of 2θ=20–80°.[78] Field-emission scanning electron microscopy (FESEM) (Tescan Mira2) was applied to understand the morphology of the products. Before FESEM measurements, the sample surface was covered with a thin gold film to prevent charge build up. X-ray photoelectron spectroscopy (XPS) was performed on an X-ray photoelectron spectrometer (ESCALAB 250; VG Scientifics) with an Al Kα irradiation source (1486.7 eV) performed at 15 kV and 10 mA. A hemispherical energy analyzer (Specs EA 10 Plus) performing in vacuum better than 10^{-7} Pa was used to determine the core-level binding energies of photoelectrons emitted from the surface. All of the peaks were deconvoluted using the SDP software program (version 4.1) with 80% Gaussian–20% Lorentzian peak fitting. All binding energy (BE) values were calibrated by fixing the C (1s) core level with a BE of 285.0 eV. Fourier-transform infrared (FTIR) spectra were documented by Bruker tensor 27 and Raman spectra of the samples were scripted by Horiba JobinYvon at λ=532 nm with a laser power of 1.7 mW, a 100× objective lens, an 0.9 NA. The Brunauer–Emmett–Teller (BET) specific surface areas of the samples were measured with BEL Belsorp-Mini II 475.[79] Adsorption–desorption isotherms of N_2 were measured at 77K. The BET surface area was calculated in the relative pressure range of P/P_0=0.05–0.2 and the pore size dimensions were calculated using the Barett–Joyner–Halenda (BJH) model.[80] Samples were degassed for 12 h at 110ºC and 10^{-6} Torr. Transmission electron microscopy (TEM) images were collected with Philips EM 208 microscope at 100 kV. The diffuse reflection spectroscopy (DRS) and absorbance of the films were recorded using Avantes Avaspec-2048-TEC spectrometer in the wavelength range of 200–900 nm. The optical band gap, Eg, can be related to the absorption coefficient, α [α=2.303 log (T/d)], d is the thickness and T is the transmission, using the Tauc expression and can be obtained by extrapolating the linear portion of $(\alpha h\upsilon)^2$ as a function of the photon energy ($h\upsilon$).[81]

2.4. Photocatalytic Measurements

Photocatalytic activity data was collected by the degradation of CO and NO_x at the ppm level in a batch-flow reactor at room temperature. TiO_2 thin film photocatalyst plates were placed in the air-tight photoreactor vessel and their positions were fixed in order to have a constant UV intensity of 3.0 mW/cm^2. The thin-film photocatalysts contribute to the apparent surface area of 50 cm^2. The vessel was placed under a UV reactor, equipped with an 8 W UV lamp

(OSRAM, Italy). One small ventilator was attached near the lamp to avoid temperature changing. The assembled system was regularly checked for leaks by means of immersing the system to the water or by applying a leak-test solution at every connection. (See Supplementary Information Figure S4).

Analytical-grade gases were acquired from a compressed-gas stainless-steel cylinder at a concentration of 1 ppm NO_x and 50 ppm CO (N_2 balance, STG gas) with traceable National Institute of Standards and Technology and National Association of Testing Authorities standards. Gas regulators were supplied from Messer. The initial concentration of NO_x was diluted to about 1 ppm and CO to 50 ppm by the air stream. The relative humidity of the flow was measured and controlled at 40%, using a water-filled Drechsel bottle. The flow rate was fixed at 200 mL/min by a mass-flow controller. After fulfilling adsorption–desorption equilibrium the lamp was turned on. The concentrations of NO_x and CO were measured by a Modular gas analyzer (GMS800 gas analyzer, SICK), which monitors NO_x and CO with a sampling rate of 0.7 L/min.[82–84]

3. Result and Discussion

3.1. Characterization

3.1.1. XRD Measurements

Fig. 1a illustrates the XRD patterns of the TiO_2 film deposited on quartz; XRD peaks are shown at 25.3°, 37.8°, and 48.6°, which confirm the anatase phase planes at (101), (004), and (200) for the nanostructured TiO_2 thin film, respectively. The maximum background signal at about 20° is due to the amorphous phase of quartz substrate.

In previous reports by other scientists, it was shown that the electronic and optical properties of the anatase phase enable it to be chosen as a photocatalyst rather than the rutile or brokite phase, which is favorable for our research strategy.[85,86]

Fig. 1b demonstrates XRD patterns of GO and FGO; in the XRD pattern of GO, a big peak could be seen (2θ=10.6°; *d*-spacing: 7.62 Å), according to the (001) diffraction peak of GO. [87-89] The large interlayer spacing (7.62 Å) of GO corresponds to the oxygen functional groups of GO such as carboxyl, hydroxyl and epoxy. The broad peak that appeared at approximately 42.5° corresponds to (101) plane of graphitic framework remains at the GO structure.[90,91]

In the XRD pattern of FGO (Fig. 1b), the main peak could be recognized at 2θ=23.79°. This gives an interlayer spacing of approximately 3.7 Å which is less small than the 7.62 Å for GO. Additionally, it has a broad shoulder at 2θ=18.5°, which was presumably induced by the bimodal or multimodal character of the interlayer spacing of FGO powder. The XRD pattern of FGO shows a broad peak centered at 2θ=16.81° (*d*-spacing: 5.27 Å), which is lower than d- spacing of GO (7.62 Å) due to functionalization.

Diffraction peaks attributed to cobalt and imidazole had a high impact on the GO surface, which is detectable by XRD and proves the functionalization of GO. In comparison, Yu et al. reported XRD results assuming the incorporation of AuNPs in GO instead of chemical bonding.[92] As well as the study on Ag-doped GO, Kim et al. observed that XRD shows no diffraction peak for silver content, indicating the dispersion of Ag in GO.[93] In our research on covalent bonding of cobalt, the diffraction peak at 2θ=10.6°, diminished in intensity, most probably because carboxylic functional groups on the surface of GO were removed after functionalization.

Fig. 1 a, b

3.1.2. FESEM and TEM Images

The FESEM image of the TiO_2 thin film (Fig. 2a) shows particle-size uniformity with small grain size (D=19.72 nm). The morphology of the particles is dense, resulting in increasing mechanical strength. The surface coating is uniform without cracks.

In the FESEM image of GO in Fig. 2b, layered structure can be observed, which consists of ultrathin and homogeneous graphene sheets. [94] Corresponding films are gently folded with ordered accumulation.

The morphology of FGO was characterized using FESEM (Fig. 2c). The FGO is porous, fluffy and irregular, layered with folded wrinkled. The FGO is rather exfoliated than GO and the outer layers are considerably delaminated. [95]

TEM image of nano-sized FGO is similar to GO with high surface area which is crucial for the catalytic purpose (Fig. 2d).[96] FGO is transparent sheet with folding edges. These wrinkles on graphene sheets are due to attachment of functional groups on both side of carbon grid.

Fig. 2 a, b, c, d

3.1.3. Nitrogen Adsorption–Desorption isotherm

Fig. 3 illustrates the nitrogen adsorption–desorption isotherm of FGO at 77K and saturated vapor pressure (P_0) of 89.785 kPa. Keeping the temperature constant and varying the external gas pressure, by recording the amount adsorbed at each pressure, the adsorption isotherm can be obtained. Pore condensation happens at a gas pressure P lower than the bulk saturated vapor pressure P_0. The isotherm of N_2 adsorption–desorption at 77 K is a typical of type IV with a hysteresis loop, which indicates the existence of uniform pore distributions. The isotherm is sharp, and the hysteresis loop at P/P_0>0.87 can be observed; therefore the catalyst is principally mesoporous, according to IUPAC classification on pores (2–50 nm). Specific surface area calculated from the BET method is 205.8 m^2 g^{-1}, average pore radius and average pore volume calculated by BJH method are 3.09 nm and 0.501 cm^3/g. The surface area of FGO (ca. 206 m^2/g) is lower than that of GO (ca. 487m^2/g). Despite the fact that, FGO has mostly sustaining its layered structure, functionalization likewise takes place at the edges of the GO particles. Therefore, parts of the basal planes near the edges snap together, owing to π–π interactions, which narrows the interlayer distance and Specific surface area decreases. The specific surface area is one of the necessary tools to individualize graphene-based materials as absorbents and catalysts.[97]

Fig. 3

3.1.4. XPS Analysis

X-ray photoelectron spectroscopy (XPS) is a practical instrument to detect the functional groups and elemental compositions. Fig. 4a demonstrates full range XPS survey of FGO. The N1s peak of FGO at 399 eV (15.5%) reveals the imidazole existence and Co2p at 779 eV (1.1%) represents cobalt presence. Successful functionalization of GO with cobalt imidazole complex was confirmed by XPS. The peak related to oxygen functional groups in the spectra

O1s (532 eV) of FGO is minor (9.5%); however, the spectrum still displays a small peak in that region, indicating a higher removal degree of oxygen-containing functional groups. The peak area calculation of C and O from the XPS survey scan in Fig. 4a reveals that the ratio of C to O atoms increased from 2.7 in GO to 7.12 in FGO, according to functionalization.

Fig. 4b shows high resolution XPS spectrum of C1s after functionalization. The noticeable, but small peak at around 288.5 eV is attributed to a small portion of carboxyl groups (1.1% of total C) in the FGO due to functionalization. The appearance of a new peak at 285.8 eV (C-N) further confirms the presence of imidazole nitrogen in the graphene sheets.

N 1s high-resolution spectra of FGO sample is shown in Fig. 4c. The deconvoluted N 1s spectrum shows three types of N atom. One at 401.0 eV correspond to N-Co, second peak at 399.8 eV stands for N-C, and the peak at 398.7 eV belongs to N=C which further confirms the chemical bonding between GO surface imidazole with Co.

Fig. 4 a, b, c

3.1.5. Raman Spectroscopy

Raman spectroscopy is a helpful instrument to characterize GOES. GO frequently engages two main aspects: a D peak at 1349 cm^{-1} and a G peak at around 1597 cm^{-1}, originating from the first-order scattering of the E2g phonon of sp^2-hybridized C atoms and a breathing mode of k-point photons with A1g symmetry, appropriately.[98] In the Raman spectrum of FGO (Fig. 5), D and G bands shifted to 1353 and 1604 cm^{-1} after GO functionalization, correspondingly. Thus, it could be deduced that the functionalization induced certain decrease in the size of in-plane sp^2 domains, increase edge planes, as well as expanding disorder in the prepared FGO.

Fig. 5

3.1.6. FTIR Spectroscopy

The FT-IR spectrum of GO in Fig. 6 indicates a broad peak at 3409 cm^{-1} in the high frequency area together with a sharp peak at 1630 cm^{-1}, corresponding to the stretching and bending vibration of water OH molecules adsorbed on GO, respectively. The peak at 846 cm^{-1} is attributed to the stretching vibration of C=O in carboxylic acid and carbonyl groups present at the edges of GO. Finally, the absorption peaks at 1223 and 1051 cm^{-1} correspond to the stretching vibration of C–O in carboxylic acids and C–OH bending of alcohol groups, respectively. The presence of these oxygen-containing groups reveals that the starting material (graphite) has been oxidized successfully.

The FTIR spectrum of FGO represents a stretching vibration of the N–H group at 2945 and 3474 cm^{-1}, depending on whether the N–H stretching is strong or broad, confirming the presence of hydrogen bonding. (Fig. 6) The stretching vibration of the C=N group of the imidazole ring is present at 1535 cm^{-1}. The peaks at 1433 and 1488 cm^{-1} represent the stretching vibrations of C=C and N=N groups, respectively, whereas the peaks at 1252 and 1325 cm^{-1} belongs to the stretching vibration of C–N=N–C and C=N–N=C. The strong band at 1065 cm^{-1} and medium band at 1094 cm^{-1} are assigned to the C–N stretching vibrations. Peaks at 853 and 937 cm^{-1} correspond to the vibration of C–N=N–C and C–N of imidazole, whereas peaks at 612, 664, and 752 cm^{-1} prove the complex formation between the cobalt and nitrogen atoms of imidazole.

Fig. 6

3.2. Optical Properties

3.2.1 UV/Vis Spectra and Band-Gap Determination

UV/Vis spectroscopy is a helpful technique for understanding photocatalyst structure. Fig. 7 displays the UV/Vis spectra of bare TiO_2, GO/TiO_2, and FGO/TiO_2 composites.

All of the samples expose sharp transition in the UV region, which could ascribed as the peculiar band-gap absorption of TiO_2, concluding that electrons transit from the valence band

to the conduction band ($O_{2p} \rightarrow Ti_{3d}$). In comparison to TiO_2 (400 nm), a redshift to higher wavelengths for GO/TiO_2 (421 nm) and FGO/TiO_2 (447 nm) composites could be inspected, proving the narrowness of band gap with the addition of GO and FGO. The approximated band gap for TiO_2, GO/TiO_2 and FGO/TiO_2 were 3.10, 2.96 and 2.77 eV, respectively. This issue supports redshift detecting in the absorption of composites, as compared to uncombined TiO_2. Bare TiO_2 exhibits no absorption above its absorption edge (400 nm), however introducing GO and FGO result in a continuous absorption band at 421–447 nm, which is in agreement with the gray–black color of the sample. Optimized absorption intensity of light for composites can lead to an enhancement in photocatalytic activity.[99,100] In the case of FGO, the reduction of band-gap energy is referred to GO carboxylic groups substitution with imidazole bonded to the cobalt.

Fig. 7

3.3. Photocatalytic Activity towards the Removal of NO_x and CO from Air

3.3.1. Photocatalyst Pre-treatment

Prior to degradation experiments, photocatalyst was illuminated by UV irradiation in presence of purified air stream (5 mL/min) in order to convert any adsorbed carbonaceous impurities, known as the carbon burn-off period.

3.3.2. Photocatalytic Activity Measurements

A setup in batch-mode adsorption experiments were performed to check out the photocatalytic degradation of NO_x and CO. The experiments were tested on three different photocatalysts, such as bare TiO_2 thin film, TiO_2/GO and TiO_2/FGO composites.

Figs. 8a and 8b display the composite photocatalysts performance for NO_x and CO degradation (C/C_0%) under UV-light irradiation. The initial concentration of CO used in this study was 50 ppm. The conversion percentage of CO as a function of residence time using the bare TiO_2 thin-film photocatalyst was calculated and is shown in Fig. 8a. Only 10% degradation of CO was found for a residence time of 120 min using the TiO_2 thin-film photocatalyst. CO degradation was 27% for TiO_2/GO composite and 46% for the TiO_2/FGO. It has probably occurred because the absorbed amount of gas on the TiO_2 thin film was rather

low. NO_x degradation ability of the TiO_2 thin film was 16%, whereas it was 31% for TiO_2/GO and 51% for TiO_2/FGO. Adding GO to the composite improves NO_x removal, though adding FGO is more effective for the same residence time. It could be seen that the existence of FGO noticeably increased the NO_x removal, because the FGO could accelerate NO adsorption, trapping VB holes and CB electrons along with complex formation with pollutant gases.

Fig. 8a, b

In the case of NO_x mixed with CO, NO_x degradation on TiO_2 thin film has not been changed, whereas for TiO_2/GO and TiO_2/FGO, it has increased by 5% and 7% consequently in the same residence time. This is probably related to GO presence. GO on one hand increases CO adsorption and photodegradation, following by elevated production of hydroxyl radicals. In the other hand, GO helps the electron–hole pair separation. In the case of TiO_2/FGO the impact of CO is more obvious than TiO_2/GO, because of more sites in cobalt structure for complex formation with pollutant gases.[101,102]

CO degradation in the presence of NO_x has not increased. It may be due to the small initial concentration of NO_x rather than CO, hence the surface saturation does not take place and there is no competition or deactivation effect between pollutant gases.[103]

Chuensab and Watcharenwong reported the photocatalytic activity of WO_3 films. The removal efficiency of CO was 45% by UV light and 31% by visible light; both cases are lower than our results.[104] Toma et al. reported 35% NO and around 20% NO_x decomposition under the optimum experiment conditions,[105] which are minor than our achievement. 23% NO_x and 34% CO removal by ZnO photocatalyst has been proposed by E. Kowsari and B. Bazri.[106] In another study, the maximum conversion efficiency of NO_2 to harmless products was 33%.[107] According to the results presented by Gomez et al., TiO_2 supported on a zeolitic composite material had acceptable degradation results; however, the formation of organophosphorous intermediates lowered the photocatalytic reaction.[108]

In case of bare TiO_2, band gap energy is 3.10 eV and when photocatalyst is irradiated with appropriate photon energy, the electrons (e_{CB}^-) and holes (h_{VB}^+) are generated in conduction and valence band, these two high energy pieces start oxidizing pollutants. Electrons react with O_2 and superoxide radicals ($O_2^{\bullet-}$) accomplish, respectively. Holes combine with water

vapor and produce hydroxyl radicals ($^{\bullet}OH$). Hydroxyl radicals attack CO and NO, resulting oxidation of pollutants (Eqs. 2-8).

CO is a poison gas, and its oxidation to CO_2 is the only feasible way for its destruction. The mechanism of CO photocatalytic oxidation is simple. Previous theoretical calculations and experiments suggested that O_2 adsorbs at the oxygen vacancy on the surface, which could be responsible for the oxidation of CO.[109]

When using TiO_2 thin film, we should pay attention to the crystal structure by preventing the electron hole recombination and adsorbing pollutants at the photocatalyst surface.

The high performance of the selected catalyst can be explained by combining TiO_2 with GO, as excited electrons of TiO_2 could move from the conduction band (CB) to graphene.[110] The barrier formed at the network termed Schottky barrier separates the electron–hole pairs, thus overcoming charge recombination. The close contact between TiO_2 and GO favors the transfer of photogenerated electrons from TiO_2 to GO, leading to an adequate charge anti-recombination and raising the photocatalytic performance (Eqs. 9-11).

$$TiO_2 + h\nu \rightarrow TiO_2 (e_{CB}^{-} + h_{VB}^{+}) \quad (2)$$

$$h_{VB}^{+} + OH_{ads}^{-} \rightarrow OH^{\bullet} \quad (3)$$

$$O_2 + e_{CB}^{-} \rightarrow O_2^{\bullet} \quad (4)$$

$$OH^{\bullet} + CO + O_2 \rightarrow CO_2 + H_2O \quad (5)$$

$$2OH^{\bullet} + NO \rightarrow H_2O + NO_2 \quad (6)$$

$$3NO_2 + 2\,OH^{\bullet} \rightarrow H_2O + NO + NO_3^{-} \quad (7)$$

$$O_2^{\bullet} + NO_x \rightarrow NO_3^{-} \quad (8)$$

$$Graphene/TiO_2 + h\nu \rightarrow Graphene\ (e_{CB}^{-})/TiO_2\ (h_{VB}^{+}) \quad (9)$$

$$Co\text{-}Im + h\nu \rightarrow Co\text{-}Im^{*}\ (excited\ state) \quad (10)$$

$$Co\text{-}Im^{*} \rightarrow Co\text{-}Im^{+} + Graphene\ (e_{CB}^{-}) \quad (11)$$

In FGO photocatalyst composite, the existence of Co-Im attachment on GO surface is crucial for preventing electron hole recombination, considering that Co-Im transfers electrons to the GO conducting band, thus the charge separation is achieved.

Zhang et al. first demonstrated the appreciated photocatalytic activity of graphene-based semiconductor composites,[111] followed by Ng,[112] Shen et al.,[113] and Zhou et al.,[114] who performed one-step hydrothermal method to supply graphene–TiO_2 hybrid materials. They presented the composite enhanced photocatalytic activity towards organic degradation

compared to bare TiO_2. Fan et al., synthesized P25-graphene composites, which illustrated significant photocatalytic performance compared to pure P25.[115]

To the best of our knowledge, this is the first study on the use of graphene functionalization with an imidazole cobalt complex-GO/TiO_2 composite on the photocatalytic degradation of CO and NO_x.

The TiO_2/FGO nanocomposite exhibits a new photocatalytic mechanism, in which cobalt acts as complexing metal and pollutant gases act as coordinating agents, according to the reaction equations (Eqs. 12–16).

This photocatalytic mechanism is specifically unusual compared to previous researches on GO–semiconductor photocatalysts, where GO is declared to behave as an electron scavenger to catch and then transport the photogenerated electrons from the semiconductor. (See Supplementary Information Figure S5)

Hard Soft Acid Base (HSAB) theory confirms that soft Lewis bases bind to soft Lewis acids, preferably and vice versa. Considering Co^{2+} as a borderline Lewis acid and carbon monoxide (CO) as a soft Lewis base, the reaction takes place. CO (Lewis base) donates a pair of electrons to Co (Lewis acid) in order to form a coordination complex. [116]

Nitric oxide is different from CO, in mechanism, because of the existence of one odd electron in an anti-bonding orbital. NO can miss one electron and become isoelectronic (NO^+) like CO. hence, cobalt complex formation with nitrosyl takes place by transmitting electrons to cobalt and forming covalence bond, respectively. Besides, NO is a strong π acceptor and can overlap with filled *d* orbitals in Co with its empty antibonding orbitals.[117]

$$[Co(Im)_4]Cl_2 + 2NO \rightarrow [Co(Im)_4(NO)_2]Cl_2 \quad (12)$$

$$[Co(Im)_4]Cl_2 + 2CO \rightarrow [Co(Im)_4(CO)_2]Cl_2 \quad (13)$$

$$[Co(Im)_4(NO)_2]Cl_2 + O_2 \rightarrow [Co(Im)_4(NO_2)_2]Cl_2 \quad (NO \rightarrow NO_2) \quad (14)$$

$$[Co(Im)_4(NO_2)_2]Cl_2 + O_2 \rightarrow [Co(Im)_4(NO_3)_2] \quad (NO_2 \rightarrow NO_3) \quad (15)$$

$$[Co(Im)_4(CO)_2]Cl_2 + O_2 \rightarrow [Co(Im)_4(CO_2)_2]Cl_2 \quad (CO \rightarrow CO_2) \quad (16)$$

XPS analysis of Co after the photocatalytic reaction confirms that Co addition can greatly enhance the chemisorptions of NO_x and CO species; at the same time, graphene can cooperate with holes, by inhibiting the recombination of photogenerated electrons and holes which lead to a photocatalytic reaction improvement.

In the case of FGO, the XPS data of Quantitative surface atomic percentage analyses of Co2p after photocatalytic reactions of CO, shows concentrations of 25% Co–C–O and 8% Co–C–(O)2 which reveals the oxidation of CO, at the cobalt surface. After the photocatalytic oxidation of NO_x , XPS results represent Co–N–O as 27%, Co–N–(O)2 as 7% and Co–N–(O)3 as 3% owing to Co–NO_x species forming (Table 1).

Table 1

Two photocatalytic reactions are considered for air pollutants removal. The first one concerns photocatalyst activity of TiO_2 for removal of NO_x and CO, whereas the other is the cobalt forms complex with CO and NO followed by the oxidation of NO to NO_2 and NO_3 as well as CO to CO_2. Both are applicable to treat dilute concentrations of CO and NO_x.

The roles of GO in this case are, first, to adsorb NO_x and CO, second, to store the species in its surface and third, to separate electrons and holes. Adding FGO to bare TiO_2 , significantly increases the NO_x and CO elimination. NO_x and CO removal per unit of FGO/ TiO_2 composite is approximately three times greater than the pure TiO_2 thin film.

4. Conclusion

In summary, a GO-based TiO_2 composite photocatalyst was developed. The anatase TiO_2 thin film was deposited on quartz substrates using RF magnetron sputtering method. FGO was composed with cobalt imidazole binding on the surface carboxylic groups of GO. The activity of the FGO/TiO_2 composite was tested by the photocatalytic degradation of NO_x and CO underneath UV irradiation. The TiO_2/FGO composite displayed high-performance photocatalytic activity as 51% for NO_x and 46% for CO, which is higher than that one achieved by GO/TiO_2 and TiO_2 thin-film. Incorporating FGO into the composite led to the decrease of band-gap and increase sensitivity to visible-light irradiation (λ>400 nm), with a superior functional properties. In addition, the photoinduced electrons can easily voyage around FGO, continuing with an efficient charge separation and a prolonging charge recombination time. These improvements, along with the increasing of the reactant adsorbing at the surface, are the key factors for augmenting the photocatalytic operation. We hope our findings could be directed to an expandable and cost-effective approach for obtaining powerful photocatalytic materials.

Acknowledgments

The authors wish to gratefully thank the Research Affairs Division at Amir Kabir University of Technology (AUT), Tehran, for financial support (Grant N.O. 4 /360).

5. References

1 S. A. Edgerton, M. W. Holdren, D. L. Smith, *J. Air Pollut. Cont. Assoc.*, 1989, **39**, 729.

2 C. W. Sweet, S. J. Vermette, *Environ. Sci. Technol*., 1992, **26**, 165.

3 R. Kostiainen, *Atmos. Environ*., 1995, **29**, 693.

4 R. Mukund, T.J. Kelly, W. Chester, *Atmos. Environ*., 1996, **30**, 3457.

5 R. M. Alberici, W. E. Jardim, *Applied Catalysis B: Environmental*., 1997, **14**, 55.

6 National Ambient Air Quality Standards (NAAQS), http://epa.gov/air/criteria.html, (accessed May 2015)

7 B. J. Finlayson-Pitts, J. N. Pitts Jr, *Science*., 1997, **267**, 1045.

8 W. Cha, S. Yun, J. Jurng, *Phys. Chem. Chem. Phys.*, 2014, **16**, 17900.

9 F. Guo, J. Yu, M. Chu, G. Xu, *Catal. Sci. Technol*., 2014, **4**, 2147.

10 F. Liu, Y. Yu, H. He, *Chem. Commun*., 2014, **50**, 8445.

11 S. Das, W. M. A. Wan Daud, *RSC Adv.*, 2014, **4**, 20856.

12 A. Fujishima, K. Honda, *Nature*., 1972, **238**, 37.

13 A. Fujishima, K. Hashimoto, T. Watanabe, BKC Inc., Tokyo, 1999, Vol. 58. pp. 14–176.

14 A. Kudo, Y. Miseki, *Chem. Soc. Rev*., 2009, **38**, 253.

15 A. Mills, S. Le Hunte, *J. Photochem. Photobiol. A Chem*., 1997, **108**, 1.

16 M. R. Hoffmann, S. T. Martin, W. Choi, D. W. Bahnemann, *Chem. Rev*., 1995, **95**, 69.

17 A. Ajmal, I. Majeed, R. N. Malik, H. Idrissc, M. A. Nadeem, *RSC Adv*., 2014, **4**, 37003.

18 U. Lavrenčič Štangar, M. Kete, A. Šuligoj, M. Tasbihi, *Mater Sci Eng*., 2012, **30**, 012001.

19 I. Arabatzis, S. Antonaraki, T. Stergiopoulos, A. Hiskia, E. Papaconstantinou, M. Bernard, *J Photochem Photobiol A Chem.,* 2002, **149**, 237.

20 K. Weng, Y. Huang, *Surf. Coat. Technol.,* 2013, **231**, 201.

21 D. Hwang, J. Moon, Y. Shul, K. Jung, D. Kim, D. Lee, *J. Sol Gel Sci. Technol.,* 2003, **26,** 783.

22 R. Fateh, A. Ismail, R. Dillert, D. Bahnemann, *J. Phys. Chem.,* 2011, **115**, 10405.

23 R. Fateh, R. Dillert, D. Bahnemann, *ACS Appl. Mater. Interface.,* 2014, **6**, 2270.

24 S. Okunaka, H. Tokudome, Y. Hitomib, R. Abe, J. *Mater. Chem. A*., 2015, **3**, 1688.

25 E. V. Skorb, D. G. Shchukin, H. Möhwald, D. V. Sviridov, *J. Mater. Chem*., 2009, **19**, 4931.

26 Z. Zhao, H. Tan, H. Zhao, D. Li, M. Zheng, P. Du, G. Zhang, D. Qu, Z. Sun, H. Fan, *Chem. Commun*., 2013, **49**, 8958.

27 D. Lee, H. Kim, S. Yu, H. J. Kim, W. I. Lee, D. Jang, *J. Mat. Sci*., 2014, **49**, 3414.

28 J. Altmayer, S. Barth, S. Mathur, *RSC Adv*., 2013, **3**, 11234.

29 R. Bhakta, R. Thomas, F. Hipler, H. F. Bettinger, J. Müller, P. Ehrhart, A. Devi, *J. Mater. Chem.,* 2004, **14**, 3231.

30 T. Nakajima, T. Nakamura, K. Shinoda, T. Tsuchiya, *J. Mater. Chem. A*., 2014, **2**, 6762.

31 R. Sellappan, J. Sun, A. Galeckas, N. Lindvall, A. Yurgens, A. Y. Kuznetsov, D. Chakarov, *Phys. Chem. Chem. Phys*., 2013, **15**, 15528.

32 J. B. Bellam, M. A. Ruiz-Preciado, M. Edely, J. Szade, A. Jouanneaux, A. H. Kassiba, *RSC Adv*., 2015, **5**, 10551.

33 S. Ameen, M. S. Akhtar, H. Seo, H. Shin. *Cryst Eng Comm*, 2014, **16**, 3020.

34 T. Sun, Y. Wang, M. Al-Mamun, H. Zhang, P. Liu, H. Zhao. *RSC Adv*., 2015, **5**, 12860.

35 H. Kim, H. Kim, W. I. Lee, D. Jang, *J. Mater. Chem. A*, 2015, **3**, 9714.

36 Q. Zeng, H. Li, H. Duan, Y. Guo, X. Liu, Y. Zhang, H. Liu, *RSC Adv*., 2015, **5**, 13430.

37 J. Yang, H. Piao, A. Vinu, A. A. Elzatahry, S. Paek, J. Choy, *RSC Adv*., 2015, **5**, 8210.

38 W. Donphai, T. Kamegawa, M. Chareonpanich, K. Nueangnoraj, H. Nishihara, T. Kyotani, H. Yamashita*, Phys. Chem. Chem. Phys*., 2014, **16**, 25004.

39 S. Zheng, L. Gao, Q. H. Zhang, J. K. Guo, *J. Mater. Chem*., 2000, **10**, 723.

40 X. D. Gao, X. M. Li, X. Y. Gan, Y. Q. Wu, R. K. Zheng, C. L. Wang, Z. Y. Gu, P. He, *J. Mater. Chem.*, 2012, **22**, 18930

41 H. He, T. Riedl, A. Lerf, J. Klinowski, *J. Phys. Chem*., 1996, **100**, 19954.

42 G. Eda, Y. Y. Lin, C. Mattevi, H. Yamaguchi, H. A. Chen, I.-S. Chen, C. W. Chen, M. Chhowalla, *Adv. Mater*., 2010, **22**, 505.

43 M. Li, S. K. Cushing, X. Zhou, S. Guo, N.Q. Wu, *J. Mater. Chem*., 2012, **22**, 23374.

44 C. Wang, J. Zhou, L. Chu*, RSC Adv*., 2015, **5**, 52466.

45 M. Barathi, A. Santhana Krishna Kumar, Chinta Uday Kumar, N. Rajesh, *RSC Adv.*, 2014, **4**, 53711.

46 Y.Li, P. Zhang, Q. Du, X. Peng, T. Liu, Z. Wang, Y. Xia, W. Zhang, K. Wang, H. Zhu, D. Wu, *J. Colloid. Interf. Sci*., 2011, **363**, 348.

47 G. Zhao, L. Jiang, Y. He, J. Li, H. Dong, X. Wang, W. Hu, *Adv. Mater*., 2011, **23**, 3959.

48 G. Zhao, J. Li, X. Wang, *Chem. Eng. J*., 2011, **173**, 185.

49 J. Wang, X. Gao, Y. Wang, C. Gao, *RSC Adv*., 2014, **4**, 57476.

50 B. Yang, Y. Guo, Sh. Zhang, T. Wen, Ch. Zhao, *RSC Adv.,* 2014**, 4**, 64771.

51 Q. Fang, B. Chen, *J. Mater. Chem. A.*, 2014, **2**, 8941-8951.

52 L. Yu, Y. Ma, C. N. Ong, J. Xie, Y. Liu, *RSC Adv.*, 2015, **5**, 64983.

53 V. Chandra, K.S. Kim, *Chem. Comm*., 2011, **47**, 3942.

54 R. Sitko, E. Turek, B. Zawisza, E. Malicka, E. Talik, J. Heimann, A. Gagor, B. Feist, R. Wrzalik*, Dalton Trans*., 2013, **42**, 5682.

55 H. Y. He, J. Klinowski, M. Forster, A. Lerf, *Chem. Phys. Lett*., 1998, **287**, 53.

56 A. Lerf, H. Y. He, M. Forster, J. Klinowski, *J. Phys. Chem. B.,* 1998, **102**, 4477.

57 H. C. Schniepp, J. L. Li, M. J. McAllister, H. Sai, M. Herrera Alonso, D. H. Adamson, R. K. Prud'homme, R. Car, D. A. Saville, I. A. Aksay, *J. Phys. Chem. B*., 2006, **110**, 8535.

58 S. Park, K. S. Lee, G. Bozoklu, W. Cai, S. T. Nguyen, R. S. Ruoff, *ACS Nano*., 2008, **2**, 572.

59 Y. Xu, Z. Liu, X. Zhang, Y. Wang, J. Tian, Y. Huang, Y. Ma, X. Zhang, Y.A. Chen, *J. Adv. Mater.,* 2009, **2**, 1275.

60 Z. B. Liu, Y. F. Xu, X. Y. Zhang, X. L. Zhang, Y. S. Chen,J. G. Tian, *J. Phys Chem B*., 2009, **113**, 9681.

61 X. Zhang, Y. Huang, Y. Wang, Y. Ma, Z. Liu, Y.Chen, *Carbon*., 2009, **47**, 334.

62 S. Wang, P. J. Chia, L. L. Chua,L. H. Zhao, R. Q. Png, S. Sivaramakrishnan, M. Zhou, R. G. S. Goh, R. H. Friend, A T. S. Wee,P. K. H. Ho, *J. Adv. Mater*., 2008, **20**, 3440.

63 H. Yang, C. Shan, F. Li, D. Han, Q. Zhang, L. Niu, *J. Chem. Comm*., 2009, **26**, 3880.

64 K. H. Cheon, J. Cho, Y. H. Kim, D. S. Chung, *ACS Appl. Mater. Interfaces*., 2015, **7**, 14004.

65 Y. Yamadaa, Y. Suzukia, H. Yasudaa, S. Uchizawaa, K. Hirose-Takai, Y. Sato, K. Suenagab, S. Satoa, *Carbon.*, 2014, **75**, 81.

66 C. Xu, X. Wang, J. Zhu, X. Yang, L. Lu, *J. Mater. Chem.*, 2008, **18**, 5625.

67 J. Wang, K. Feng, H. H. Zhang, B. Chen, Z. J. Li, Q. Y. Meng, L. P. Zhang, C. H. Tung, L. Z. Wu., *Beilstein J. Nanotechnol.* 2014**, 5***,* 1167.

68 L. Wang, D. Wang, X. Hu, J. Zhu, X. Liang, *Electrochimica Acta*., 2012, **76**, 282.

69 S. Losse, J. G. Vos, S. Rau, *Coord. Chem. Rev*., 2010, **254**, 2492.

70 J. Tian, H. Li, A. Asiri, A. Al-Youbi, X. Sun, *small*., 2013, **9**, 2709.

71 X. Dong, H. Xu, X. Wang, Y. Huang, M. Chan-Park, H. Zhang, L. Wang, W. Huang, P. Chen, *ACS Nano*., 2012, **6**, 3206.

72 H. Yu, Z. Tan, *Environ. Sci. Techno*., 2014, DOI: 10.1021/ES403901R.

73 W. Cruz, P. Leung, K. Seff, *Inorg Chem*., 1979, **18**, 1692.

74 Y. Lee, Y. Kim, K. Seff, *J Phys Chem B*., 2005, 109, 4900.

75 O. Alnaji, M. Dartiguenave, Y. Dartiguenave, M. Simard, A. Beauchamp, *Inorganica Chimica Acta.*, 1991, **187**, 31.

76 W.S. Hummers, R.E. Offeman, *J. Am. Chem. Soc*., 1958, **80**, 1339.

77 J. T. Robinson, M. Zalalutdinov, J. W. Baldwin, E. S. Snow, Z. Wei P. Sheehan, B. H. Houston, *Nano Lett*., 2008, **8**, 3441.

78 C. Suryanarayana, M. Grant Norton, *X-Ray Diffraction: A Practical Approach*, Plenum Press, New York, 1998.

79 K.S.W. Sing, D.H. Everett, R.A.W. Haul, L. Moscou, R.A. Pierotti, J. Rouquerol, T. Siemieniewska, *Pure Appl. Chem*., 1985, **57**, 603.

80 F. Rouquerol, J. Rouquerol, K. Sing, *Adsorption by Powders & Porous Solids*, Academic Press, London, 1999.

81 J. Tauc, *Optical Properties of Solids*, North-Holland, Amsterdam, 1972, pp. 278-313.

82 C.H. Huang, I. K. Wang, Y. M. Lin, Y.H. Tseng, C. M. Lu, *J. Mol. Catal. A: Chemical*., 2010, **316**, 163.

83 ISO 22197-1: 2007, 'Fine ceramics, advanced technical ceramics) – Test method for air-purification performance of semiconducting photocatalytic materials – part 1: Removal of nitric oxide, ISO, Geneva, 2007.

84 ISO 10677: 2011, Fine ceramics, advanced technical ceramics –Ultraviolet light source for testing semiconducting photocatalytic materials, ISO, Geneva, 2011.

85 J. N. Hart, D. Menzies, Y. B. Cheng, G. P. Simon, L. Spiccia, *Sol Energ Mat Sol C*., 2007, **91**, 6.

86 H. Kim, D. Jang, *Cryst Eng Comm*., 2015, **17**, 3325.

87 X. Li, Y. Hu, J. Liu, A. Lushington, R. Li, X. Sun, *Nanoscale*., 2013, **5**, 12607.

88 X. Tong, H. Wang, G. Wang, L. Wan, Z. Ren and J. Bai, *J. Solid State Chem*., 2011, **184**, 982.

89 A. Buchsteiner, A. Lerf, J. Pieper, *J Phys Chem B*., 2006, **110**, 22328.

90 Q. Du, M. Zheng, L. Zhang, Y. Wang, J. Chen, L. Xue, W. Dai, G. Ji, J. Cao, *Electrochim. Acta*., 2010, **55**, 3897

91 Z. Xu, Y. Huang, C. Min, L. Chen, *Radiat Phys Chem*., 2010, **79**, 839.

92 H. Yu, P. Xu, D.W. Lee , X. Li, *J. Mater. Chem. A*., 2013, **1**, 4444.

93 K. S. Kim, I. J. Kim, S. J. Park, *Synthetic Met*., 2010, **160**, 2355.

94 M. Chhowalla, G. Eda, *Adv. Mater.,* 2010, **22**, 2392.

95 Y. Zhu, S. Murali, W. Cai, Li X, J. W. Suk, J. R. Potts R.S. Ruoff, *Adv Mater*., 2010, **22**, 3906.

96 C. Zhu, S. Guo, Y. Fang, S. Dong, *ACS Nano*., 2010, **4**, 2429.

97 Q. Yu, L.A. Jauregui, W. Wu, R. Colby, J. Tian, Z. Su, H. Cao, Z. Liu, D. Pandey, D. Wei, T.F. Chung, P. Peng, N.P. Guisinger, E.A. Stach, J. Bao, S. Pei, Y.P. Chen, *Nature Mater*., 2011, **10**, 443.

98 S. Pisana, M. Lazzeri, C. Casiraghi, K.S. Novoselov, A.K. Geim, A.C. Ferrari, F. Mauri, *Nature Mater*., 2007, **6**, 198.

99 H. Yamashita, M. Harada, J. Misaka, M. Takeuchi, K. Ikeue, M. Anpo, *Journal of Photochemistry and Photobiology A: Chemistry*., 2002, **148**, 257

100 S. G. Babu, R. Vinoth, D. P. Kumar, M. V. Shankar, H. Chou, K. Vinodgopal, B. Neppolian, *Nanoscale.*, 2015, **7**, 7849.

101 O. Carp, C.L. Huisman, A. Reller, *Solid State Chem.*, 2004, **32**, 33.

102 M.L. Sauer, D.F. Ollis, *J. Catal*., 1996, **163**, 215.

103 C.H. Ao, S.C. Lee, C.L. Mak, L.Y. Chan, *Applied Catalysis B: Environmental*.,2003, **42**, 119.

104 A. Chuensab, A.Watcharenwong, International Conference on Chemical, Environmental and Biological Sciences (ICCEBS), Malaysia, 2012.

105 F. L. Toma, G. Bertrand, D. Klein, C. Coddet, *Environ Chem Lett*., 2004, **2**, 117.

106 E. Kowsari, B. Bazri, *Applied Catalysis A: General*., 2014, **475**, 325.

107 A. Gandolfo, V. Bartolomei, E. Gomez Alvarez, S. Tlili, S. Gligorovskia, J. Kleffmann, H. Wortham, *Applied Catalysis B: Environmental*., 2015, **166**, 84.

108 S. Gomez, C. Leal Marchena, M. S. Renzini, L. Pizzio, L.Pierella, *Applied Catalysis B: Environmental.,* 2015, **162**, 167.

109 A. V. Vorontsov, E. N. Savino, E. N. Kurkin, O. D. Torbova, V. N. Parmon, *Catal Lett*., 1997, **62**, 83-88.

110 G. Williams, B. Seger,P. V. Kamat, *ACS Nano*., 2008, **2**, 1487-1491.

111 H. Zhang, X. Lv, Y. Li, Y. Wang, J. Li, *ACS Nano*., 2009, **4**, 380.

112 Y. H. Ng , I. V. Lightcap , K. Goodwin , M. Matsumura, P. V. Kamat, *J. Phys. Chem. Lett*., 2010, **15**, 2222.

113 J. Shen, B. Yan, M. Shi, H. Ma, N. Li, M. Ye, *J. Mater. Chem*., 2011, **21**, 3415.

114 K. Zhou, Y. Zhu, X. Yang, X. Jiang, C. Li, *New. J. Chem.*, 2011, **35**, 353.

115 W. Fan, Q. Lai, Q. Zhang, Y. Wang, *J. Phys. Chem C.*, 2011, **115**, 10694.

116 Organomettalic Hyper Text Book, http://www.ilpi.com/organomet/carbonyl.html (accessed June 2015)

117 P. T. Manoharan and H. B. Gray, Inorg. Chem., 1966, ch. 5, P. 823

Captions for Figures

Fig. 1a) XRD pattern of TiO_2 thin film. b) XRD plots of GO and FGO.

Fig. 2 a) FESEM photograph top surface TiO_2 thin film. b) FESEM image of GO. c) FESEM image of FGO and d) TEM image of FGO.

Fig. 3 N_2 adsorption–desorption isotherm of FGO at 77K and Saturated vapor pressure (P_0= 89.785 kPa) with the hysteresis loop at P/P_0>0.87.

Fig. 4 a) XPS survey spectrum of FGO and b) XPS C1s region spectrum for FGO with the results of curve fitting c) N1s region of FGO with the results of curve fitting

Fig. 5 Raman spectra of FGO.

Fig. 6 FTIR spectra of GO and FGO.

Fig. 7 UV/Vis spectra of the TiO_2 thin film, TiO_2/GO, and TiO_2/FGO composites.

Fig. 8 a) Degradation of CO with irradiation time over the samples under UV-light irradiation and b) Degradation of NO_x with irradiation time over the samples under UV-light irradiation.

Table Caption

Table 1. XPS elementary atomic surface ratios of the FGO catalyst before and after the photocatalytic reactions.

Table 1

Sample	Atomic ratios (%)							
	Co–N=C	Co–N–C	Co–Cl	Co–C–O	Co–C–(O)2	Co–N–O	Co–N–(O)2	Co–N–(O)3
FGO before photocatalytic reactions	45	39	26	--	--	--	--	--
FGO after photocatalytic reactions of CO	30	35	10	25	8	--	--	--
FGO after photocatalytic reactions of NO_x	28	33	2	--	--	27	7	3

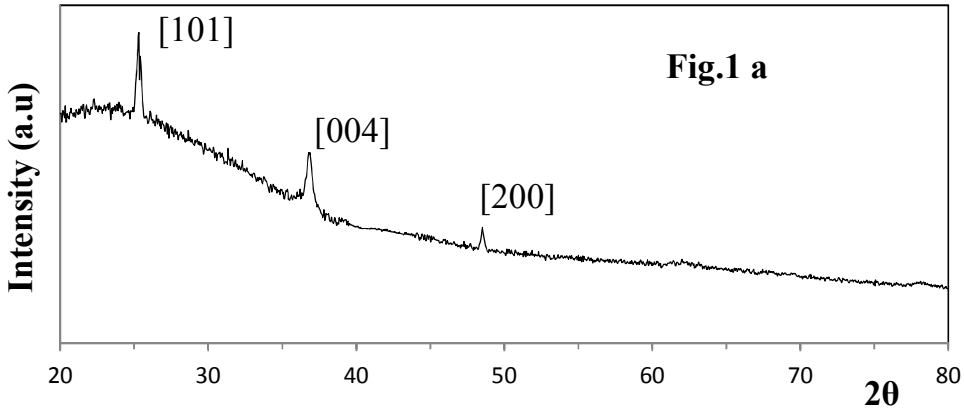

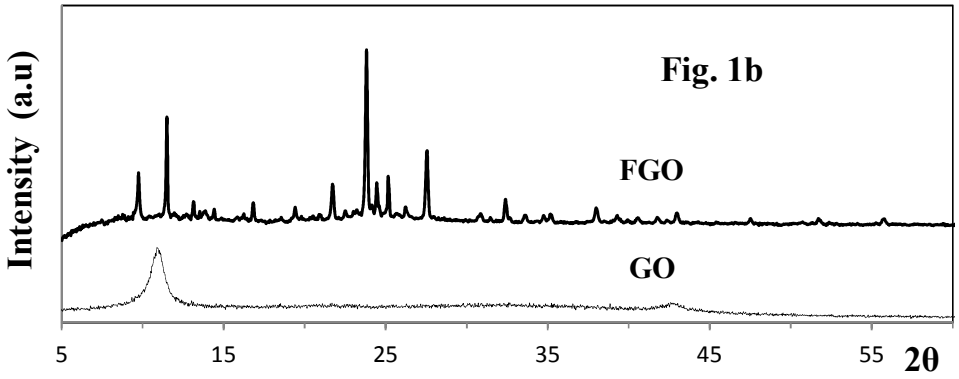

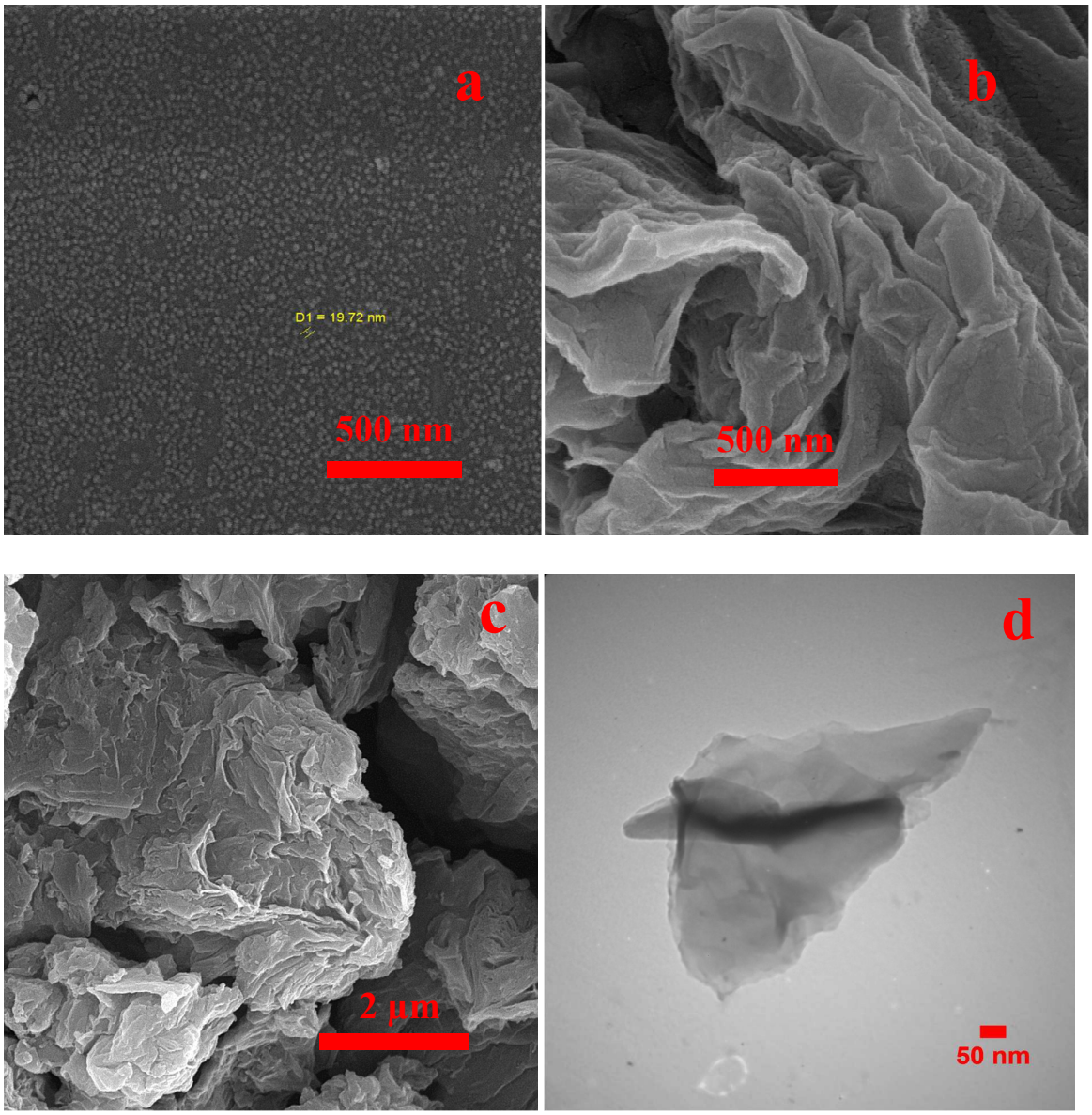

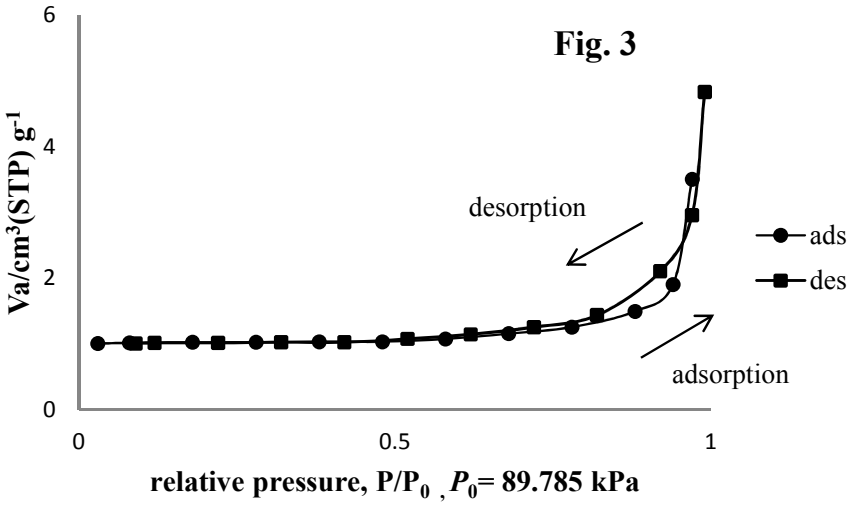

Fig. 3

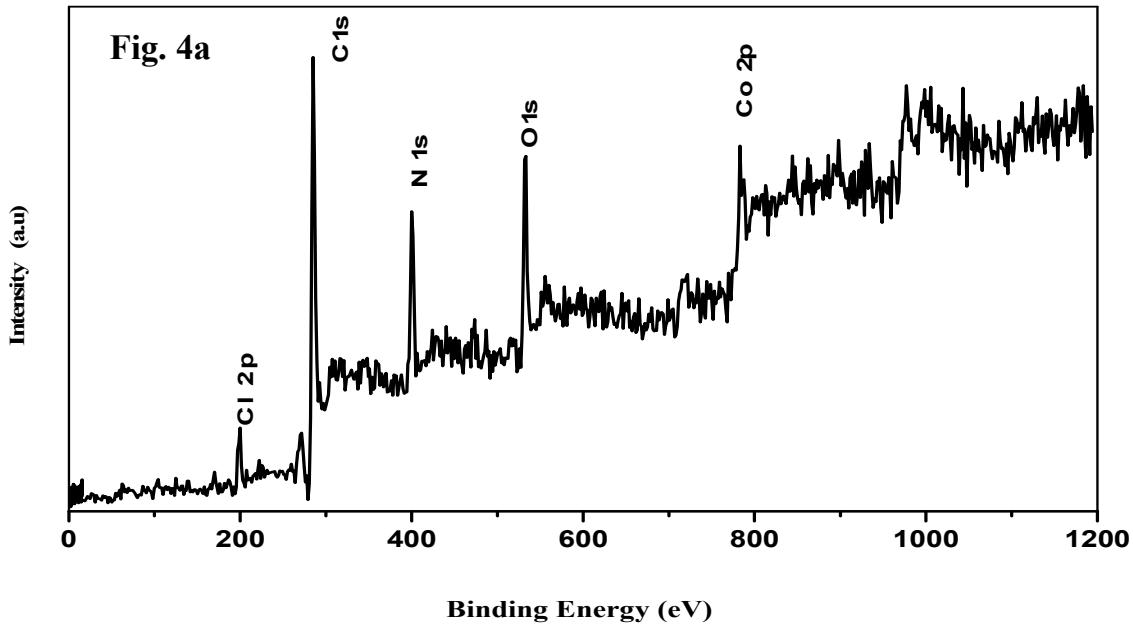

Fig. 4b

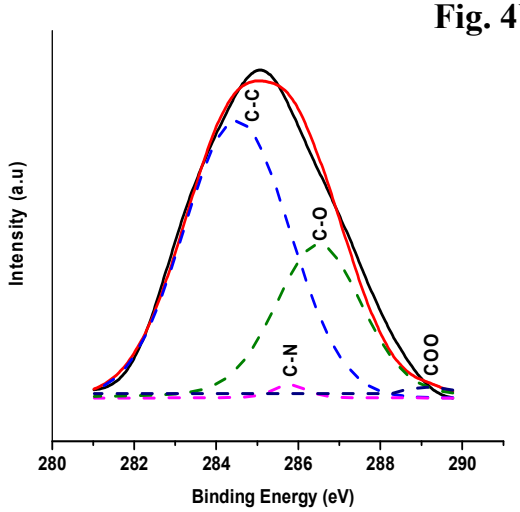

Fig. 4c

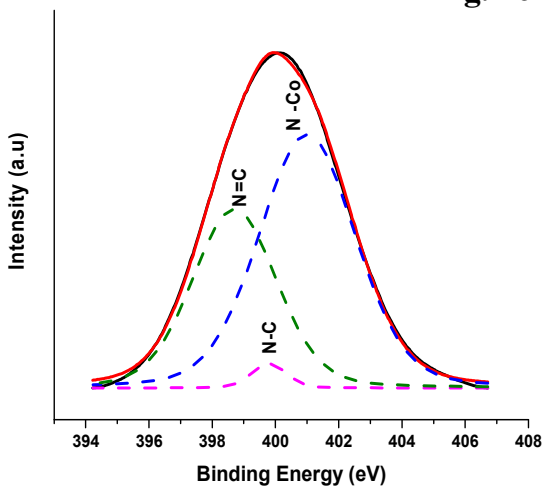

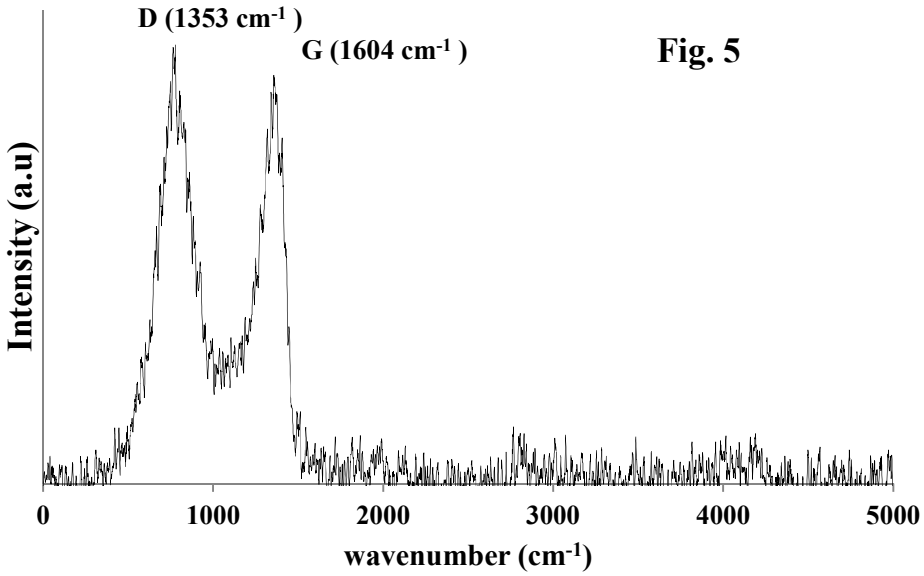

Fig. 5

Fig. 6

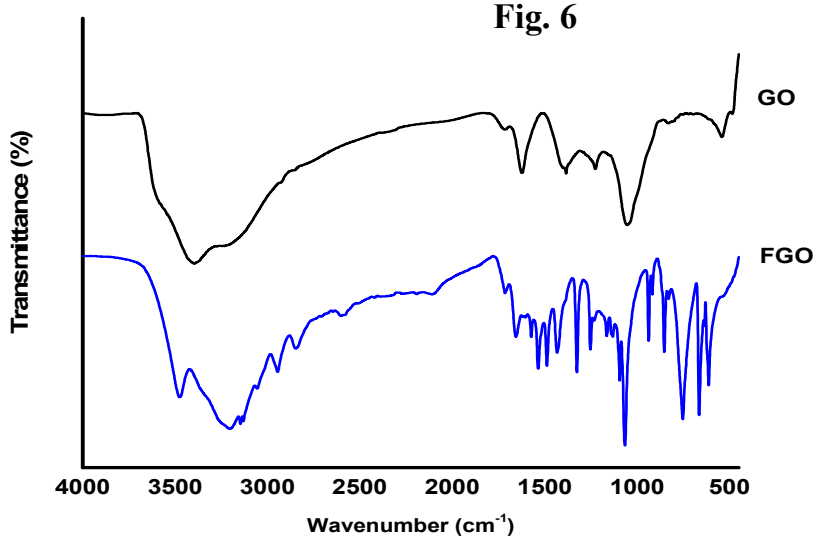

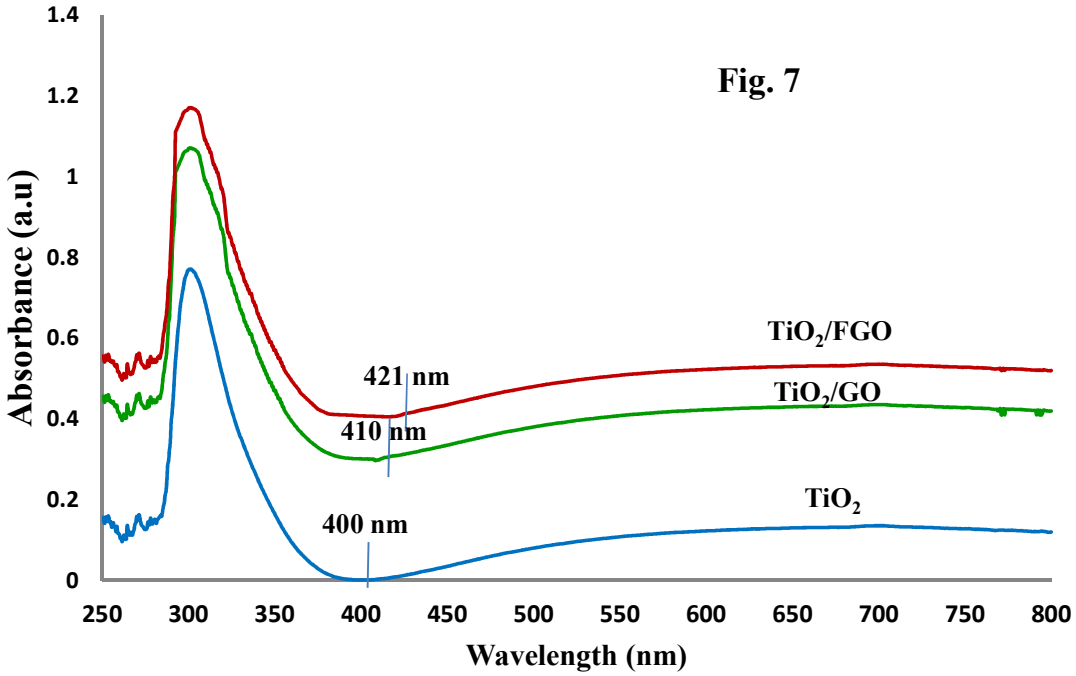

Fig. 7